A metabolism-based quorum sensing mechanism contributes to termination of inflammatory responses

Jérémy Postat, Romain Olekhnovitch, Fabrice Lemaître, Philippe Bousso

A metabolism-based quorum sensing mechanism contributes to termination of inflammatory responses

Jérémy Postat[1,2,3], Romain Olekhnovitch[1,2,3], Fabrice Lemaître[1,2] and Philippe Bousso[1,2,4,*]

[1] Dynamics of Immune Responses Unit, Institut Pasteur, 75015 Paris, France
[2] INSERM U1223, 75015 Paris, France
[3] University Paris Diderot, Sorbonne Paris Cité, Cellule Pasteur, rue du Dr Roux, 75015 Paris, France
[4] Lead Contact

[*] Correspondence to: philippe.bousso@pasteur.fr

Summary

Recruitment of immune cells with antimicrobial activities is essential to fight local infections but has the potential to trigger immunopathology. Whether the immune system has the ability to sense inflammation intensity and self-adjust accordingly to limit tissue damage remains to be fully established. During local infection with an intracellular pathogen, we have shown that nitric oxide (NO) produced by recruited monocyte-derived cells was essential to limit inflammation and cell recruitment. Mechanistically, we have provided evidence that NO dampened monocyte-derived cell cytokine and chemokine production by inhibiting cellular respiration and reducing cellular ATP:ADP ratio. Such metabolic control operated at the tissue level but only when a sufficient number of NO producing cells reached the site of infection. Thus, NO production and activity act as a quorum sensing mechanism to help terminate the inflammatory response.

Introduction

Infection with pathogens and tissue damage triggers inflammation, a dynamic process aimed at protecting the injured host. Soluble mediators produced in particular by macrophages and mast cells actively increase vascular permeability and attract immune cells with antimicrobial properties (Medzhitov, 2008). However, overwhelming inflammation may be responsible for severe immunopathology often due to excessive neutrophil accumulation. Mechanisms to terminate inflammation are therefore essential for balancing antimicrobial activity and tissue damage.

While the decrease in pathogen load or injury may help limit inflammation, active mechanisms implicating immune cells and mediators have also been shown to suppress the inflammatory reaction (Ortega-Gomez et al., 2013; Sugimoto et al., 2016). These include processes to decrease neutrophil activity and numbers through induction of apoptosis and increased clearance, mechanisms to regulate cytokine and chemokine activity by reactive oxygen species (ROS) generation or through truncation and sequestration by decoy receptors. Additionally, macrophage transition from a pro-inflammatory to a pro-resolving state represents an important step for terminating immune responses. Despite this important knowledge, mechanisms that select the appropriate time for inflammation resolution are poorly understood. Specifically, whether a mechanism exists to sense when a sufficient number of immune cells have accumulated to elicit the termination of inflammation remains unknown.

To address these questions, we took advantage of the self-resolving cutaneous infection with *Leishmania major* parasites (Sacks and Noben-Trauth, 2002; Scott and Novais, 2016) as a

physiological model to study inflammation termination. Local infection with this intracellular pathogen triggers the massive recruitment of monocyte-derived mononuclear phagocytes (thereafter referred to as monocyte-derived cells), that not only represents the major populations of infected cells but are also actively involved in fighting the infection (De Trez et al., 2009; Leon et al., 2007; Olekhnovitch et al., 2014). Efficient immune responses indeed rely on inducible nitric oxide synthase (iNOS, NOS2)-mediated nitric oxide (NO) production by monocyte-derived cells, promoted by interferon-γ (IFN-γ) producing $CD4^+$ T cells (Olekhnovitch and Bousso, 2015; Sacks and Noben-Trauth, 2002; Scott and Novais, 2016). NO production has a direct effect on the parasite, limiting its proliferation and survival (Liew et al., 1990; Muller et al., 2013). However, decreasing parasite load may not be sufficient to stop the inflammatory reaction raising the possibility that additional mechanisms acting on immune cells are important to terminate the response. Notably, NO displays immunoregulatory properties (Bogdan, 2001; Giustizieri et al., 2002; Kobayashi, 2010; Lu et al., 2015; Mishra et al., 2013; Speyer et al., 2003; Thomassen et al., 1997) suggesting that it can act not only on the pathogen but also on inflammatory cells at the site of infection. In addition, recent studies have indicated that NO can modify cellular metabolism in *in vitro* settings (Everts et al., 2012; Van den Bossche et al., 2016). However, by which mechanisms NO could influence the inflammatory response *in vivo* remains to be fully established. In particular, the relevance of NO impact on metabolism *in vivo* has yet to be demonstrated. Finally, the spatiotemporal activity of NO in tissues is largely unknown.

Here, we have shown that NO production acts to adjust and limit the intensity of the inflammatory response. We have established that NO suppresses monocyte-derived cell accumulation as well as cytokine and chemokine production by blocking cellular respiration and decreasing ATP:ADP ratio. Such mechanism required a high density of recruited iNOS-

expressing cells and acted at the tissue level through NO diffusion. Thus, monocyte-derived cells not only produce NO but are also regulated in number and activity by the amount of this molecule in the environment, establishing a quorum sensing mechanism for the control of inflammatory responses.

Results

NO dampens the inflammatory reaction at the site of *L. major* infection

During infection with intracellular pathogens, host NO can exert pleiotropic effects influencing immune responses at multiple stages (Bogdan, 2015; Olekhnovitch and Bousso, 2015). To specifically evaluate the impact of NO production on an established inflammatory reaction, we assessed the consequence of a short period of iNOS inhibition in *L. major* infected mice (**Figure 1A**). We used the specific iNOS chemical inhibitor L-NIL and treated mice 2 weeks post infection for 3 days. We found that iNOS inhibition profoundly increased myeloid cell numbers at the site of infection, with a major effect on neutrophils and monocyte-derived cells (**Figure 1B**). We and others have previously shown that Ly6C^{+}MHC-II^{-} monocytes (P1 population) are massively recruited at the site of infection and further differentiate into Ly6C^{+}MHC-II^{+} (P2 population) and subsequently into Ly6C^{-}MHC-II^{+} cells (P3 population) (Leon et al., 2007; Olekhnovitch et al., 2014). All three populations of mononuclear phagocytes were substantially increased upon a short inhibition of iNOS (**Figure 1B**). To extend these results, we used *Lyz2*$^{+/EGFP}$ mice (in which both neutrophils and macrophages are labeled with GFP) to visualize the effect of iNOS inhibition on myeloid cell density at the site of infection. Consistent with our flow cytometric analysis, two-photon imaging of the ear dermis revealed a significant increase in the density of myeloid cells (GFP^{+}) upon transient iNOS inhibition (**Figure 1C**). We next investigated the effect of iNOS inhibition on the inflammatory milieu at the site of infection by analyzing cytokine and chemokine concentrations in total ear tissue. We observed an overall increase in cytokine concentrations when iNOS activity was blocked. The effect appeared very broad and concerned most of the cytokines tested, including IL-1α, IL-1β, TNF-α, IL-6, IL-12 (p40 and p70), IL-10, IL-5, IL-4 (**Figure 1D**). Similarly, iNOS inhibition led to a dramatic increase in chemokine concentrations in the ear tissue, including CXCL1, CXCL10, CCL2, CCL3

(**Figure 1D**). Altogether, our results indicate that NO production at the site of *L. major* infection controls, either directly (acting on cells) or indirectly (acting on the pathogen), the inflammatory reaction, limiting immune cell infiltrates together with cytokine and chemokine concentrations.

NO impacts myeloid cell recruitment at the site of *L. major* infection

To specifically assess the role of NO on immune cell recruitment at the site of infection, we performed adoptive transfer of myeloid populations by injecting fluorescently-labeled bone marrow cells in infected mice. Cell recruitment in the infected ear was assessed in the presence or absence of iNOS inhibition (**Figure 2A**). Using intravital imaging, we detected the recruitment of transferred cells at the site of infection with a marked increase in GFP^+ cell numbers upon suppression of iNOS activity (**Figure 2B**). We confirmed this result using flow cytometry with a significant enhancement of myeloid cell (including neutrophils) recruitment upon iNOS inhibition (**Figure 2C**). Notably, a sizable fraction (~6%) of newly recruited cells including neutrophils and monocyte-derived cells became infected in wild-type mice during this short window of time (**Figure 2D**). Our results suggest that the constant recruitment of myeloid cells contributes to fuel *L. major* infection and, most importantly, that iNOS activity limits such a self-sustained process.

NO restricts monocyte-derived cells function *in vivo* at the single cell level

Having shown that NO limits the overall cytokine production in the infected tissue, we asked whether this effect was uniquely due to a reduced accumulation of cytokine-producing immune cells or whether NO exerted an additional effect on immune cell activity. We focused on monocyte-derived cells, the major population of myeloid cells at the site of infection and analyzed cytokine production at the single cell level, in infected mice upon transient

inhibition of iNOS (**Figure 3A**). As shown in **Figure 3B-C**, we observed an increased percentage of TNF-α-producing cells as well as an increased cytokine production on a per cell basis in infected mice in which iNOS activity was suppressed. This effect was not specific to TNF-α since we obtained similar results by analyzing the production of two other cytokines: pro-IL-1β and CCL3 (**Figure 3C**). Similar effects were observed when either total or infected cells were analyzed (**Figure S1A-B**). These results indicate that NO produced by monocyte-derived cells at the site of infection dampens their ability to produce cytokines and chemokines. When assessing the effects of L-NIL treatment, we found that a 3-days inhibition of iNOS also increased the percentage of infected monocyte-derived cells (**Figure S1C-D**). While this could be the result of the increased immune cell recruitment at the site of infection, it could also reflect NO antimicrobial activity. Therefore, it was important to test whether NO mediated its effects indirectly by influencing pathogen load or by direct alteration of cellular activity. To test the latter possibility, we analyzed how NO affects monocyte-derived cell activity in a non-infectious model of inflammation using emulsified incomplete Freund's adjuvant (**Figure S2A**). In this model, we observed massive recruitment of myeloid cells including the three aforementioned mononuclear phagocytes populations (P1, P2, P3) and a robust induction of iNOS (**Figure S2B-C**). Importantly, treatment with L-NIL increased monocyte-derived cell activity as measured by TNF-α, CCL2 and CCL3 production (**Figure S2D**). These results suggest that NO can restrict monocyte-derived cell activity independently of any potential effect on pathogen burden

NO broadly restricts bone marrow-derived macrophages functions *in vitro*

To further confirm and dissect the direct effect of NO on immune cells, we activated WT or *Nos2*$^{-/-}$ bone marrow-derived macrophages *in vitro* and in the absence of pathogen with LPS+IFN-γ, a treatment that induces iNOS expression in WT cells. As shown in **Figure 4A**,

LPS+IFN-γ treatment induced the intracellular production of the tested cytokines (pro-IL-1β and CCL2) in both WT and *Nos2*$^{-/-}$ macrophages. However, cytokine production was significantly higher in *Nos2*$^{-/-}$ macrophages. We repeated these experiments by treating WT macrophages with L-NIL to suppress NO production in order to exclude any potential additional defect of cells isolated from *Nos2*$^{-/-}$ mice. Consistently, we observed higher production of pro-IL-1β and CCL2 in the presence of iNOS inhibition (**Figure 4B**). As expected, L-NIL had no effects on *Nos2*$^{-/-}$ macrophages or on WT unactivated macrophages (**Figure S3**). We extended the aforementioned results obtained with intracellular cytokine staining by performing multi-analyte cytokine profiling on macrophage supernatants. Reflecting the effect of iNOS inhibition during *L. major* infection, *Nos2*$^{-/-}$ macrophages exhibited an overall increased production of inflammatory cytokines and chemokines, including IL-1α, IL-1β, IL-6, CXCL10, CCL2, CCL3 (**Figure 4C**). These results suggest that NO acts on macrophages to limit cytokine and chemokine production both *in vitro* and *in vivo*.

NO blockade of mitochondrial respiration restricts ATP:ADP ratio and macrophage activity

Given the broad suppression of cytokine production by NO, we asked whether this effect could originate from a change in cellular metabolism (Biswas and Mantovani, 2012; Everts et al., 2012; Lu et al., 2015; Na et al., 2018; Sancho et al., 2017; Thwe and Amiel, 2018; Van den Bossche et al., 2016; Van den Bossche et al., 2017). Consistent with this idea, we observed that WT macrophages engage glycolysis but stop relying on oxidative phosphorylation upon activation as measured by decreased basal respiration and ATP synthesis (**Figure 5A-B**). By contrast, *Nos2*$^{-/-}$ macrophages used both respiration and glycolysis upon activation (**Figure 5A-B**). Overall, glycolytic activity and glucose uptake

were not affected by iNOS activity (**Figure S4**). Similarly, blocking iNOS activity with L-NIL in WT macrophages restored their respiratory capacity when activated (**Figure 5C**). To confirm these findings at the single cell level, we used a combination of dyes to measure total (MitoTracker GreenFM) and respiring (MitoTracker Red CMXRos) mitochondria by flow cytometry. A drop in cell respiration was seen upon activation of WT but not *Nos2*$^{-/-}$ macrophages (**Figure S5A**). Again, blocking iNOS activity in WT macrophages was sufficient to restore respiration (**Figure S5B**). To test whether these findings pertain to monocyte-derived cells *in vivo* at the site of *L. major* infection, we sorted monocyte-derived cells from the ears of infected WT mice and subjected them to metabolic flux analysis in the presence or absence of L-NIL. As observed with *in vitro* macrophages, *ex vivo*-isolated WT monocyte-derived cells displayed a block in respiration that was relieved by a short incubation (2h) with L-NIL (**Figure 5D**). These results demonstrate that NO production by macrophages drastically suppresses their respiratory capacity, in both bone marrow-derived macrophages and monocyte-derived cells at the site of infection.

To further characterized the impact of NO on cellular metabolism, we relied on PercevalHR, a genetically-encoded fluorescent probe for monitoring ATP:ADP ratio hence providing a readout for the energetic status of individual cells in real-time (Tantama et al., 2013). Upon NO exposure, we observed a drop in ATP:ADP ratio in activated and L-NIL-treated PercevalHR-expressing macrophages within less than 10 minutes, as measured by time-resolved flow cytometry (**Figure 6A**). These findings were confirmed by following individual PercevalHR-expressing macrophages using live-imaging (**Figure 6B**). Thus, one important consequence of NO targeting of mitochondrial respiration is the rapid and substantial reduction in the cellular ATP:ADP ratio. We next ask whether such energetic changes could explain the reduced cytokine production in macrophages exposed to NO. We therefore specifically inhibited the ATP synthase using oligomycin (that targets the F0 subunit of the

ATP synthase). We noted that oligomycin treatment induced a drop in ATP:ADP ratio similar to that observed with NO (**Figure 6C-D**). Most importantly, a short term (4 h) inhibition of ATP synthase in macrophages was sufficient to reduce cytokine and chemokine production as measured by intracellular cytokine staining (**Figure 6E**) and multi-analyte cytokine profiling (**Figure 6F**). Similar results were observed by performing the experiment in hypoxic condition **(Figure S6A**) or by blocking respiration with azide that targets complex IV of the mitochondrial respiratory chain, which activity precedes that of the ATP synthase **(Figure S6B**). Together, our results support the idea that NO blockade of mitochondrial respiration rapidly diminishes the cellular energetic resources required for optimal cytokine production. To test whether NO also affect the ATP:ADP ratio *in vivo* during infection, we generated chimeric mice by transducing HSCs with PercevalHR and infected them with *L. major* (**Figure 6G**). Two weeks later, we measured the ATP:ADP ratio in monocyte-derived cells at the infection site in mice treated or not with L-NIL. We observed that iNOS inhibition largely increased cellular ATP:ADP ratio in both P2 and P3 populations (**Figure 6H**) supporting the relevance of our model during inflammation *in vivo*.

Collective NO production provides a quorum-sensing mechanism to dampen chronic inflammation

We next sought to clarify how NO acts in the infected tissue. NO could act in a cell-autonomous manner, suppressing the respiration of individual NO-producing cells or act more broadly by diffusing in the tissue. In addition, it was unclear whether NO produced by a single cell has any biological activity or whether the collective production by numerous cells is essential to impact on cellular metabolism.

We first addressed these questions *in vitro* by mixing iNOS competent and deficient macrophages at different ratios to generate distinct densities of NO producing cells at a

constant total cell number. We found that the block of cell respiration in macrophages increased with density of NO-producing cells (**Figure S5C-E**). Most importantly, only a modest block in cell respiration was seen in macrophages competent for NO production when these cells were present at low density (10:90 ratio), indicating that the effect on cellular metabolism was by large not cell-intrinsic. Conversely, a block in respiration was detected in *Nos2*$^{-/-}$ macrophages provided that they were surrounded by numerous iNOS competent cells (50:50 ratio) (**Figure S5C-E**). Importantly, the same rules applied for cytokine and chemokine production (**Figure S5F-G**). Indeed, pro-IL-1β and CCL2 production was suppressed in both WT and *Nos2*$^{-/-}$ macrophages mixed at 50:50 ratio. At lower ratio (10:90), pro-IL-1β and CCL2 production were largely unaffected even in WT macrophages. These results strongly suggest that the density of NO-producing cells plays a crucial role to regulate cell activity (**Figure S5**).

To test this hypothesis *in vivo*, we generated mixed-bone marrow chimeras using various ratios of WT (CD45.1) and *Nos2*$^{-/-}$ (CD45.2) cells for reconstitution (**Figure 7A-B**) in order to establish varying densities of iNOS competent cells at the infection site. The corresponding cellular densities were estimated by intravital imaging (**Figure S7A-C**). Following infection with *L. major*, we assessed the activity of monocyte-derived cells isolated at the site of infection. Our results revealed that the amount of pro-IL-1β (**Figure 7C, Figure S7D**) produced was regulated by the density of iNOS competent cells. Moreover, the amounts of cytokine production were identical in WT (CD45.1) and *Nos2*$^{-/-}$ (CD45.2) cells analyzed in the same environment, indicating that NO-mediated effect on cytokine production is not cell-intrinsic but instead largely rely on NO diffusion in the tissue. Similar results were obtained analyzing TNF-α (**Figure 7D, Figure S7D**) and CCL3 (**Figure 7E, Figure S7D**) production. Therefore, NO mediates the downregulation of the inflammatory reaction only when a sufficient number of NO-producing cells have accumulated at the site of infection. We

estimated that a density of approximately 5000 iNOS competent cells/mm^3 need to be reach to substantially inhibit cytokine production (**Figure S7D**). Furthermore, NO acts at the tissue level through diffusion irrespectively of intrinsic iNOS expression.

In sum, monocyte-derived cells that accumulate at the site of infection produce diffusible NO that will progressively inhibit further recruitment and inflammation as cell density increases. Monocyte-derived cells are therefore endowed with a metabolism-based quorum-sensing mechanism to help control and terminate the immune response.

Discussion

In the present report, we identified a novel mechanism that adjusts the intensity of the inflammatory reaction to the local density of monocyte-derived cells. Mechanistically, we have shown that nitric oxide decreased cellular respiration, ATP:ADP ratio and cytokine and chemokine production, dampening myeloid cell recruitment and overall inflammation. Since NO was found to act only when a sufficient number of NO-producing cells have accumulated, these properties define a quorum-sensing mechanism for the control and termination of inflammatory reactions.

In the context of infection with an intracellular pathogen, we confirmed that the role of NO extends beyond its well-known antimicrobial properties by profoundly influencing immune cell activity *in vivo*. *Nos2*$^{-/-}$ mice have been previously shown to exhibit exacerbated immunopathology in response to infection with *L. major* or *M. tuberculosis* (Belkaid et al., 2000; Mishra et al., 2017; Mishra et al., 2013; Wei et al., 1995). Since iNOS deficiency may affect the initiation and development of the immune response, we used a short pharmacological inhibition of iNOS to reveal the role of NO specifically once the inflammatory reaction is established. Blocking NO production for 3 days was sufficient to boost monocyte-derived cell ability to secrete cytokines and chemokines at the single cell level and to increase myeloid cell recruitment and accumulation. Such an enhanced recruitment of myeloid cells could possibly originate from factors derived from monocytes and/or neutrophils, two cell types that that act in concert during inflammation (Dal-Secco et al., 2015; Kreisel et al., 2010; Lammermann et al., 2013). In addition, NO could influence cell recruitment by modulating leukocyte adhesion and extravasation (Banick et al., 1997; Kubes et al., 1991). In agreement with previous studies (Bogdan, 2001; Braverman and Stanley,

2017; Eigler et al., 1995; Giustizieri et al., 2002; Speyer et al., 2003; Thomassen et al., 1997), these observations were recapitulated on *in vitro* derived-macrophages in the absence of pathogen, suggesting that the observed effects of NO on the immune reaction were not simply due to indirect changes in the parasite. NO-mediated suppression of cytokine production can result from an alteration of inflammasome assembly (Mishra et al., 2013) or a decrease in NF-κB activity (Braverman and Stanley, 2017; Matthews et al., 1996). Notably, in our model, NO appeared to decrease cytokine and chemokine production very broadly, affecting most type-1, type-2 and suppressive cytokines tested.

The wide range of cytokines and chemokines downregulated by NO prompted us to investigate a global effect on cellular metabolism. NO has the ability to block the respiratory chain (Brown, 1999, 2001; Clementi et al., 1998) and iNOS induction has been shown to block respiration in dendritic cells and macrophages cultured *in vitro* (Van den Bossche et al., 2016) or in inflammatory dendritic cells stimulated *ex vivo* (Everts et al., 2012). To extend these findings, we sought to determine whether blockade of respiration by NO could be observed in an ongoing immune response. By directly analyzing the metabolism of sorted monocyte-derived cells from the site of *L. major* infection, we showed that these cells exhibited a profound block in cell respiration that could be reversed by a short inhibition of iNOS. Using a genetically-encoded reporter for ATP:ADP ratio (PercevalHR), we noted that NO decreased the cellular energetic yield both *in vitro* and *in vivo*. These observations establish the physiological relevance of NO-mediated alteration of cell metabolism in the context of a chronic inflammation with an intracellular pathogen. Importantly, we provide evidence that respiration blockade and decrease in ATP production are by themselves sufficient to limit cytokine and chemokine production suggesting a causal link between NO-mediated respiration blockade and dampening of monocyte-derived cell activity.

While our data support a role for NO in reducing cytokine production by altering respiration and energetic yield, additional mechanisms could also contribute to limit inflammation. These include mitochondria-dependent mechanisms such as modulation of mitochondrial ROS (Mills et al., 2016) and/or concentrations of specific metabolites (e.g succinate (Mills et al., 2016; Tannahill et al., 2013) and itaconate (Cordes et al., 2016; Lampropoulou et al., 2016; Michelucci et al., 2013)) but also mitochondria-independent mechanisms such as modulation of NADPH oxidase-derived ROS (Bagaitkar et al., 2015; Harbort et al., 2015; Meissner et al., 2008; Morgenstern et al., 1997; Warnatsch et al., 2017) and/or alteration of the NF-κB pathway (Braverman and Stanley, 2017; Matthews et al., 1996).

Collectively, results from this work and from other studies (Amiel et al., 2014; Everts et al., 2012; Van den Bossche et al., 2016) highlight the diverse effects of respiration blockade by NO on monocyte-derived cell biology, including alteration of survival capacity, plasticity and inflammatory activity.

One key result of our study is that the impact of NO on monocyte-derived cell metabolism is not a cell-autonomous mechanism requiring intrinsic iNOS expression. Instead, it is the number of NO-producing cells in the microenvironment that determines the respiratory capacity of monocyte-derived cells at the tissue level, affecting similarly NO-producing and non-producing cells, most likely through diffusion. In other contexts, cytokine may similarly act both on producing and non-producing cells to coordinate heterogeneous populations in a given environment (Shalek et al., 2014). We have previously observed such a dependency on collective NO production and NO diffusion to mediate antimicrobial activity (Olekhnovitch et al., 2014). *In vitro* experiments have delineated the various impact of iNOS induction on macrophages and dendritic cells (Everts et al., 2012; Lu et al., 2015; Van den Bossche et al., 2016). Our results suggest that it is important to consider that these effects are not necessarily

cell-autonomous and can vary drastically *in vivo* based on the density of iNOS-expressing cells in the microenvironment. In this respect, we estimated that the suppressive effects of NO were substantial when the density of monocyte-derived cells reached 5000 cells/mm^3 in the skin.

Quorum-sensing mechanisms allow bacteria to sense and react to the density of their population, with the help of a diffusible mediator termed auto-inducer (Miller and Bassler, 2001). Similar mechanisms may exist in the immune system at homeostasis or during immune responses. For example, IgG secreted by activated B cells has been shown to regulate B cell homeostasis (Montaudouin et al., 2013). Here, we show that monocyte-derived cells can modify their activity and recruitment by sensing their density through the release of the diffusible molecule NO. We therefore propose that quorum-sensing is integral to the inflammatory reaction, allowing to temporally control immune cell numbers and activity for optimal immune responses with limited immunopathology.

Acknowledgments

We thank C. Demangel and members of the Bousso laboratory for critical review of the manuscript. We acknowledge the mouse facility and Technology Core of the Center for Translational Science (CRT) at Institut Pasteur for support in conducting this study and the specific contribution of B. Charbit, T. Stephen, S. Novault and S. Schmutz. The work was supported by Institut Pasteur, Inserm, and by a Starting (Lymphocytecontact) and an Advanced Grant (ENLIGHTEN) from the European Research Council.

Author contributions

J.P. conducted the experiments. F.L. generated reagents, J.P., R.O. and P.B. designed the experiments and analyzed the data. J.P. and P.B. wrote the manuscript.

Competing financial interests

The authors declare no competing financial interest.

References

Amiel, E., Everts, B., Fritz, D., Beauchamp, S., Ge, B., Pearce, E.L., and Pearce, E.J. (2014). Mechanistic target of rapamycin inhibition extends cellular lifespan in dendritic cells by preserving mitochondrial function. J Immunol *193*, 2821-2830.

Bagaitkar, J., Pech, N.K., Ivanov, S., Austin, A., Zeng, M.Y., Pallat, S., Huang, G., Randolph, G.J., and Dinauer, M.C. (2015). NADPH oxidase controls neutrophilic response to sterile inflammation in mice by regulating the IL-1alpha/G-CSF axis. Blood *126*, 2724-2733.

Banick, P.D., Chen, Q., Xu, Y.A., and Thom, S.R. (1997). Nitric oxide inhibits neutrophil beta 2 integrin function by inhibiting membrane-associated cyclic GMP synthesis. J Cell Physiol *172*, 12-24.

Belkaid, Y., Mendez, S., Lira, R., Kadambi, N., Milon, G., and Sacks, D. (2000). A natural model of Leishmania major infection reveals a prolonged "silent" phase of parasite amplification in the skin before the onset of lesion formation and immunity. J Immunol *165*, 969-977.

Biswas, S.K., and Mantovani, A. (2012). Orchestration of metabolism by macrophages. Cell Metab *15*, 432-437.

Bogdan, C. (2001). Nitric oxide and the immune response. Nature immunology *2*, 907-916.

Bogdan, C. (2015). Nitric oxide synthase in innate and adaptive immunity: an update. Trends Immunol *36*, 161-178.

Braverman, J., and Stanley, S.A. (2017). Nitric Oxide Modulates Macrophage Responses to Mycobacterium tuberculosis Infection through Activation of HIF-1alpha and Repression of NF-kappaB. J Immunol *199*, 1805-1816.

Brown, G.C. (1999). Nitric oxide and mitochondrial respiration. Biochim Biophys Acta *1411*, 351-369.

Brown, G.C. (2001). Regulation of mitochondrial respiration by nitric oxide inhibition of cytochrome c oxidase. Biochim Biophys Acta *1504*, 46-57.

Clementi, E., Brown, G.C., Feelisch, M., and Moncada, S. (1998). Persistent inhibition of cell respiration by nitric oxide: crucial role of S-nitrosylation of mitochondrial complex I and protective action of glutathione. Proc Natl Acad Sci U S A *95*, 7631-7636.

Cordes, T., Wallace, M., Michelucci, A., Divakaruni, A.S., Sapcariu, S.C., Sousa, C., Koseki, H., Cabrales, P., Murphy, A.N., Hiller, K.*, et al.* (2016). Immunoresponsive Gene 1 and Itaconate Inhibit Succinate Dehydrogenase to Modulate Intracellular Succinate Levels. J Biol Chem *291*, 14274-14284.

Dal-Secco, D., Wang, J., Zeng, Z., Kolaczkowska, E., Wong, C.H., Petri, B., Ransohoff, R.M., Charo, I.F., Jenne, C.N., and Kubes, P. (2015). A dynamic spectrum of monocytes arising from the in situ reprogramming of CCR2+ monocytes at a site of sterile injury. J Exp Med *212*, 447-456.

De Trez, C., Magez, S., Akira, S., Ryffel, B., Carlier, Y., and Muraille, E. (2009). iNOS-producing inflammatory dendritic cells constitute the major infected cell type during the chronic Leishmania major infection phase of C57BL/6 resistant mice. PLoS pathogens *5*, e1000494.

Eigler, A., Moeller, J., and Endres, S. (1995). Exogenous and endogenous nitric oxide attenuates tumor necrosis factor synthesis in the murine macrophage cell line RAW 264.7. J Immunol *154*, 4048-4054.

Everts, B., Amiel, E., van der Windt, G.J., Freitas, T.C., Chott, R., Yarasheski, K.E., Pearce, E.L., and Pearce, E.J. (2012). Commitment to glycolysis sustains survival of NO-producing inflammatory dendritic cells. Blood *120*, 1422-1431.

Giustizieri, M.L., Albanesi, C., Scarponi, C., De Pita, O., and Girolomoni, G. (2002). Nitric oxide donors suppress chemokine production by keratinocytes in vitro and in vivo. Am J Pathol *161*, 1409-1418.

Harbort, C.J., Soeiro-Pereira, P.V., von Bernuth, H., Kaindl, A.M., Costa-Carvalho, B.T., Condino-Neto, A., Reichenbach, J., Roesler, J., Zychlinsky, A., and Amulic, B. (2015). Neutrophil oxidative burst activates ATM to regulate cytokine production and apoptosis. Blood *126*, 2842-2851.

Kobayashi, Y. (2010). The regulatory role of nitric oxide in proinflammatory cytokine expression during the induction and resolution of inflammation. J Leukoc Biol *88*, 1157-1162.

Kreisel, D., Nava, R.G., Li, W., Zinselmeyer, B.H., Wang, B., Lai, J., Pless, R., Gelman, A.E., Krupnick, A.S., and Miller, M.J. (2010). In vivo two-photon imaging reveals monocyte-dependent neutrophil extravasation during pulmonary inflammation. Proc Natl Acad Sci U S A *107*, 18073-18078.

Kubes, P., Suzuki, M., and Granger, D.N. (1991). Nitric oxide: an endogenous modulator of leukocyte adhesion. Proc Natl Acad Sci U S A *88*, 4651-4655.

Lammermann, T., Afonso, P.V., Angermann, B.R., Wang, J.M., Kastenmuller, W., Parent, C.A., and Germain, R.N. (2013). Neutrophil swarms require LTB4 and integrins at sites of cell death in vivo. Nature *498*, 371-375.

Lampropoulou, V., Sergushichev, A., Bambouskova, M., Nair, S., Vincent, E.E., Loginicheva, E., Cervantes-Barragan, L., Ma, X., Huang, S.C., Griss, T.*, et al.* (2016). Itaconate Links Inhibition of Succinate Dehydrogenase with Macrophage Metabolic Remodeling and Regulation of Inflammation. Cell Metab *24*, 158-166.

Leon, B., Lopez-Bravo, M., and Ardavin, C. (2007). Monocyte-derived dendritic cells formed at the infection site control the induction of protective T helper 1 responses against Leishmania. Immunity *26*, 519-531.

Liew, F.Y., Millott, S., Parkinson, C., Palmer, R.M., and Moncada, S. (1990). Macrophage killing of Leishmania parasite in vivo is mediated by nitric oxide from L-arginine. J Immunol *144*, 4794-4797.

Lu, G., Zhang, R., Geng, S., Peng, L., Jayaraman, P., Chen, C., Xu, F., Yang, J., Li, Q., Zheng, H.*, et al.* (2015). Myeloid cell-derived inducible nitric oxide synthase suppresses M1 macrophage polarization. Nat Commun *6*, 6676.

Matthews, J.R., Botting, C.H., Panico, M., Morris, H.R., and Hay, R.T. (1996). Inhibition of NF-kappaB DNA binding by nitric oxide. Nucleic Acids Res *24*, 2236-2242.

Medzhitov, R. (2008). Origin and physiological roles of inflammation. Nature *454*, 428-435.

Meissner, F., Molawi, K., and Zychlinsky, A. (2008). Superoxide dismutase 1 regulates caspase-1 and endotoxic shock. Nat Immunol *9*, 866-872.

Michelucci, A., Cordes, T., Ghelfi, J., Pailot, A., Reiling, N., Goldmann, O., Binz, T., Wegner, A., Tallam, A., Rausell, A.*, et al.* (2013). Immune-responsive gene 1 protein links metabolism to immunity by catalyzing itaconic acid production. Proc Natl Acad Sci U S A *110*, 7820-7825.

Miller, M.B., and Bassler, B.L. (2001). Quorum sensing in bacteria. Annu Rev Microbiol *55*, 165-199.

Mills, E.L., Kelly, B., Logan, A., Costa, A.S.H., Varma, M., Bryant, C.E., Tourlomousis, P., Dabritz, J.H.M., Gottlieb, E., Latorre, I.*, et al.* (2016). Succinate Dehydrogenase Supports Metabolic Repurposing of Mitochondria to Drive Inflammatory Macrophages. Cell *167*, 457-470 e413.

Mishra, B.B., Lovewell, R.R., Olive, A.J., Zhang, G., Wang, W., Eugenin, E., Smith, C.M., Phuah, J.Y., Long, J.E., Dubuke, M.L.*, et al.* (2017). Nitric oxide prevents a pathogen-permissive granulocytic inflammation during tuberculosis. Nat Microbiol *2*, 17072.

Mishra, B.B., Rathinam, V.A., Martens, G.W., Martinot, A.J., Kornfeld, H., Fitzgerald, K.A., and Sassetti, C.M. (2013). Nitric oxide controls the immunopathology of tuberculosis by inhibiting NLRP3 inflammasome-dependent processing of IL-1beta. Nat Immunol *14*, 52-60.

Montaudouin, C., Anson, M., Hao, Y., Duncker, S.V., Fernandez, T., Gaudin, E., Ehrenstein, M., Kerr, W.G., Colle, J.H., Bruhns, P.*, et al.* (2013). Quorum sensing contributes to activated IgM-secreting B cell homeostasis. J Immunol *190*, 106-114.

Morgenstern, D.E., Gifford, M.A., Li, L.L., Doerschuk, C.M., and Dinauer, M.C. (1997). Absence of respiratory burst in X-linked chronic granulomatous disease mice leads to abnormalities in both host defense and inflammatory response to Aspergillus fumigatus. J Exp Med *185*, 207-218.

Muller, A.J., Aeschlimann, S., Olekhnovitch, R., Dacher, M., Spath, G.F., and Bousso, P. (2013). Photoconvertible pathogen labeling reveals nitric oxide control of Leishmania major infection in vivo via dampening of parasite metabolism. Cell host & microbe *14*, 460-467.

Na, Y.R., Je, S., and Seok, S.H. (2018). Metabolic features of macrophages in inflammatory diseases and cancer. Cancer Lett *413*, 46-58.

Olekhnovitch, R., and Bousso, P. (2015). Induction, Propagation, and Activity of Host Nitric Oxide: Lessons from Leishmania Infection. Trends in parasitology *31*, 653-664.

Olekhnovitch, R., Ryffel, B., Muller, A.J., and Bousso, P. (2014). Collective nitric oxide production provides tissue-wide immunity during Leishmania infection. The Journal of clinical investigation *124*, 1711-1722.

Ortega-Gomez, A., Perretti, M., and Soehnlein, O. (2013). Resolution of inflammation: an integrated view. EMBO Mol Med *5*, 661-674.

Sacks, D., and Noben-Trauth, N. (2002). The immunology of susceptibility and resistance to Leishmania major in mice. Nat Rev Immunol *2*, 845-858.

Sancho, D., Enamorado, M., and Garaude, J. (2017). Innate Immune Function of Mitochondrial Metabolism. Front Immunol *8*, 527.

Scott, P., and Novais, F.O. (2016). Cutaneous leishmaniasis: immune responses in protection and pathogenesis. Nat Rev Immunol *16*, 581-592.

Shalek, A.K., Satija, R., Shuga, J., Trombetta, J.J., Gennert, D., Lu, D., Chen, P., Gertner, R.S., Gaublomme, J.T., Yosef, N.*, et al.* (2014). Single-cell RNA-seq reveals dynamic paracrine control of cellular variation. Nature *510*, 363-369.

Speyer, C.L., Neff, T.A., Warner, R.L., Guo, R.F., Sarma, J.V., Riedemann, N.C., Murphy, M.E., Murphy, H.S., and Ward, P.A. (2003). Regulatory effects of iNOS on acute lung inflammatory responses in mice. Am J Pathol *163*, 2319-2328.

Sugimoto, M.A., Sousa, L.P., Pinho, V., Perretti, M., and Teixeira, M.M. (2016). Resolution of Inflammation: What Controls Its Onset? Front Immunol *7*, 160.

Tannahill, G.M., Curtis, A.M., Adamik, J., Palsson-McDermott, E.M., McGettrick, A.F., Goel, G., Frezza, C., Bernard, N.J., Kelly, B., Foley, N.H.*, et al.* (2013). Succinate is an inflammatory signal that induces IL-1beta through HIF-1alpha. Nature *496*, 238-242.

Tantama, M., Martinez-Francois, J.R., Mongeon, R., and Yellen, G. (2013). Imaging energy status in live cells with a fluorescent biosensor of the intracellular ATP-to-ADP ratio. Nat Commun *4*, 2550.

Thomassen, M.J., Buhrow, L.T., Connors, M.J., Kaneko, F.T., Erzurum, S.C., and Kavuru, M.S. (1997). Nitric oxide inhibits inflammatory cytokine production by human alveolar macrophages. Am J Respir Cell Mol Biol *17*, 279-283.

Thwe, P.M., and Amiel, E. (2018). The role of nitric oxide in metabolic regulation of Dendritic cell immune function. Cancer Lett *412*, 236-242.

Van den Bossche, J., Baardman, J., Otto, N.A., van der Velden, S., Neele, A.E., van den Berg, S.M., Luque-Martin, R., Chen, H.J., Boshuizen, M.C., Ahmed, M.*, et al.* (2016). Mitochondrial Dysfunction Prevents Repolarization of Inflammatory Macrophages. Cell Rep *17*, 684-696.

Van den Bossche, J., O'Neill, L.A., and Menon, D. (2017). Macrophage Immunometabolism: Where Are We (Going)? Trends Immunol *38*, 395-406.

Warnatsch, A., Tsourouktsoglou, T.D., Branzk, N., Wang, Q., Reincke, S., Herbst, S., Gutierrez, M., and Papayannopoulos, V. (2017). Reactive Oxygen Species Localization Programs Inflammation to Clear Microbes of Different Size. Immunity *46*, 421-432.

Wei, X.Q., Charles, I.G., Smith, A., Ure, J., Feng, G.J., Huang, F.P., Xu, D., Muller, W., Moncada, S., and Liew, F.Y. (1995). Altered immune responses in mice lacking inducible nitric oxide synthase. Nature *375*, 408-411.

Figure legends

Figure 1. NO dampens the inflammatory reaction at the site of *L. major* infection.

(A) Experimental set-up. WT mice were infected with DsRed-expressing *L. major* and treated 14 days later with the specific iNOS inhibitor L-NIL. Inflammatory reaction in infected ears was characterized 3 days later. **(B)** *Top*. Flow cytometry contour plots showing the gating strategy used to analyze mononuclear phagocytes (P1, P2 and P3) from extracted ear cells. *Bottom*. Absolute cell numbers of myeloid cells, neutrophils and mononuclear phagocytes in infected ears from untreated (blue circles) or L-NIL-treated (orange circles) WT mice as assessed by flow cytometry. A third of the ear cell preparation was used flow cytometric analysis and 200000 cells were acquired. Representative of 6 independent experiments. **(C)** *Left*. Representative images of two-photon intravital imaging performed on infected ears from untreated or L-NIL-treated *Lyz2*$^{+/EGFP}$ mice, showing DsRed-expressing *L. major* and myeloid cells (GFP^{+}). Scale bar: 50 μm. *Right*. Quantification of GFP fluorescence in infected ears from untreated or L-NIL-treated mice. Results are representative of 2 independent experiments. **(D)** Cytokines (IL-1α, IL-1β, TNF-α, IL-6, IL-12 (p40 and p70), IL-4, IL-5 and IL-10) and chemokines (CXCL10, CXCL1, CCL2 and CCL3) quantification in ear lysates from untreated (blue bars) or L-NIL-treated (orange bars) mice as assessed by multiplex assay. Ears from age and sex-matched uninfected mice were analyzed to assess cytokine basal concentrations. Results are representative of 3 independent experiments. Data are represented as mean ± SD.

Figure 2. NO impacts immune cell recruitment at the site of *L. major* infection

(A) Experimental set up. WT mice were infected with DsRed-expressing *L. major* and treated 14 days later with the specific iNOS inhibitor L-NIL. Cell recruitment was assessed 3 days

later by transferring i.v. fluorescently-labeled bone marrow cells. **(B)** *Left*. Representative images of two-photon intravital imaging performed on infected ears from untreated or L-NIL-treated mice, showing DsRed-expressing *L. major* (red), Evans blue-labeled vessels (magenta) and GFP^+ extravasated cells (green). Scale bar: 100 μm. *Right*. The absolute numbers of extravasated cells in the imaging field were measured for untreated (blue bar) or L-NIL-treated (orange bar) mice. Representative of 2 independent experiments. **(C)** Percentages and absolute cell numbers of total GFP^+ cells and GFP^+ neutrophils in infected ears from untreated (blue circles) and L-NIL-treated (orange circles) mice as assessed by flow cytometry. **(D)** *Top*. Contour plot and quantification of infection among recruited GFP^+ cells in untreated mice. *Bottom*. Pie chart showing the cellular composition of infected cells among the recruited GFP^+ cells. Results are representative of 6 independent experiments. Data are represented as mean ± SD.

Figure 3. NO restricts monocyte-derived cells function *in vivo* at the single cell level.

(A) Experimental set-up. WT mice were infected with DsRed-expressing *L. major* and treated 14 days later with the specific iNOS inhibitor L-NIL. Monocyte-derived cell activity (P2 and P3 gates) was assessed 3 days later by intracellular cytokine staining on isolated ear cells. **(B)** Contours plots showing TNF-α staining in monocyte-derived cells from untreated or L-NIL-treated mice. Percentages and gMFI (in brackets) of producing cells are shown in respective plots. **(C)** Percentages (bars) and gMFI (scatter dot plots) of TNF-α-, pro-IL-1β- or CCL3-producing monocytes-derived cells (P2 and P3 gates) from untreated (blue) and L-NIL-treated (orange) mice as assessed by flow cytometry. Results are representative of 2 independent experiments with 6 ears analyzed per group and per experiment. Data are represented as mean ± SD. *See also Figure S1 and S2.*

Figure 4. NO broadly restricts bone-marrow derived macrophage functions *in vitro*.

WT or *Nos2*$^{-/-}$ BMDMs were activated 24 h with LPS+IFN-γ or left unactivated. **(A)** Percentages and gMFI of pro-IL-1β (left) and CCL2 (right) producing WT (blue bars) or *Nos2*$^{-/-}$ (orange bars) cells as assessed using intracellular cytokine staining. Representative of 4 independent experiments. **(B)** Percentages and gMFI of pro-IL-1β- (left) and CCL2- (right) producing BMDMs cultured in the absence (blue bars) or presence (orange bars) of L-NIL. **(C)** Cytokines (IL-1α, IL-1β, IL-6) and chemokines (CXCL10, CCL2 and CCL3) quantification in WT or *Nos2*$^{-/-}$ BMDM supernatants as assessed by multiplex assay. Results are representative of 2 independent experiments with 6 replicates per conditions and per experiment. Data are represented as mean ± SD. *See also Figure S3 and S5.*

Figure 5. NO dampens mitochondrial respiration *in vitro* and *in vivo*.

(A,B) WT or *Nos2*$^{-/-}$ BMDMs were activated 24 h with LPS+IFN-γ or left unactivated before extracellular flux analysis. **(A)** Oxygen consumption rate (OCR) measured during sequential treatments with oligomycin, FCCP and rot/antA on WT and *Nos2*$^{-/-}$ BMDMs. **(B)** Quantification of ATP synthesis and basal respiration based on OCR variations for WT (blue bars) and *Nos2*$^{-/-}$ (orange bars) BMDMs. Basal OCR and ECAR are graphed for the indicated populations to represent their metabolic phenotypes. Representative of 3 independent experiments. **(C)** *Left*. OCR was measured on untreated or L-NIL-treated WT activated BMDMs. *Right*. Quantification of ATP synthesis and basal respiration based on OCR variations for untreated (blue bars) or L-NIL-treated WT (orange bars) activated BMDMs. **(D)** *Left*. OCR was measured on monocyte-derived cells isolated from infected ears. Cells were left untreated or treated with L-NIL for 2 h *ex vivo*. *Right*. Quantification of basal

respiration, maximal respiration and spare respiratory capacity (SRC) based on OCR variations for untreated (blue bars) or L-NIL-treated (orange bars) cells. Results were evaluated using a two-tailed unpaired Student's t-test with Welch's correction. Results are representative of six mice analyzed in 2 independent experiments. Data are represented as mean ± SD. *See also Figure S4 and S5*

Figure 6. NO alters ATP:ADP ratio *in vitro* and *in vivo*, restricting macrophage activity. (**A-D**) Single-cell measurement of ATP:ADP ratio in BMDMs. PercevalHR-expressing BMDMs were activated 24 h with LPS+IFN-γ in the presence of L-NIL. (**A**) ATP:ADP ratio was measured in BMDMs immediately following incubation with the NO donor SNAP (100 μM) (or DMSO as a control) by time-resolved flow cytometry. Normalized cellular ATP:ADP ratio was calculated using PercevalHR fluorescence measured at λ_{low} = 405 nm and λ_{high} = 488 nm excitation wavelengths (see Experimental procedure). The graph shows the geometric mean for the normalized ATP:ADP ratio as a function of the acquisition time. (**B**) Live-imaging of ATP:ADP ratio in BMDMs exposed to SNAP (100 μM) using two-photon excitation (λ_{low} = 830 nm and λ_{high} = 1040 nm). Quantification for multiple cells (left) and representative time-lapse images (right) are shown. (C) ATP:ADP ratio was measured in BMDMs immediately following incubation with the ATP synthase inhibitor oligomycin (1 μM) (or DMSO as a control) by time-resolved flow cytometry. (D) Live-imaging of ATP:ADP ratio in BMDMs exposed to oligomycin (1 μM). Results are representative of three independent experiments. (**E-F**) BMDMs were activated 24 h with LPS+IFN-γ in the presence or in the absence of L-NIL or left untreated. When indicated BMDMs were incubated with various concentration of oligomycin for the last 4 h of the culture. (**E**) Percentages of cytokine-producing cells were assessed by intracellular cytokine staining for pro-IL-1β, CCL2 and CCL3. Representative of 3 independent experiments. (**F**) Cytokines and

chemokines in BMDM supernatants cultured in the presence or absence of oligomycin were measured by multiplex assay. Medium was changed in all samples at the time of oligomycin addition. (**G-H**) NO decreases ATP:ADP ratio in monocyte-derived cells *in vivo*. (G) Experimental set-up. Chimeric mice reconstituted with PercevalHR HSCs were infected with *L. major*. Two weeks later, some mice were treated with L-NIL for 3 consecutive days. Monocyte-derived cells recovered at the site of infection were analyzed for ATP:ADP ratio (based on PercevalHR fluorescences) by flow cytometry. (**H**) Representative histograms (left) and bar plot (right) of the ATP:ADP ratio in P2 and P3 populations recovered from infected mice with or without iNOS inhibition. Results were evaluated using a two-tailed unpaired Student's t-test with Welch's correction. Data are represented as mean ± SD. *See also Figure S6.*

Figure 7. Collective NO production provides a quorum-sensing mechanism to dampen inflammation.

(A) Experimental set-up. CD45.1 WT recipient mice were lethally irradiated and reconstituted with CD45.1 WT and CD45.2 *Nos2*$^{-/-}$ bone marrow cells, mixed at different ratios. Chimeras were infected 6 weeks later with DsRed-expressing *L. major*. Monocyte-derived cells activity was assessed 17 days later by intracellular cytokine staining on extracted ear cells. **(B)** Cellular composition in the ear of infected mixed-bone marrow chimeras. (**C-E**) Percentages (top) and gMFI (bottom) of pro-IL-1β- **(C)**, TNF-α- **(D)** and CCL3- **(E)** producing Ly6C^{+} MHC-II^{+} monocyte-derived cells (P2 gate) among the overall population (100:0 (blue bars), 0:100 (orange bars), mixed chimeras (black bars)) as assessed by intracellular cytokine staining. The inset shows the analysis of WT (CD45.1) and *Nos2*$^{-/-}$ (CD45.2) cells in the same chimeric mice prepared at the indicated WT:*Nos2*$^{-/-}$ ratio.

Representative of 7 mice per group in 2 independent experiments. Data are represented as mean ± SD. *See also Figure S7.*

STAR Methods Text

Contact for reagent and resource sharing

Further information and requests for resources and reagents should be directed to and will be fulfilled by the Lead Contact, Philippe Bousso (philippe.bousso@pasteur.fr)

Experimental model and subject details

Mice

C57BL/6J mice were obtained from Charles River France. C57BL/6J-Ptprc[a] (CD45.1), C57BL/6J-Tg(UBC-GFP)30Scha/J (Ubi-GFP), C57BL/6J-*Lyz2*$^{tm1.1Graf[EGFP]}$ (*Lyz2*$^{+/EGFP}$), C57BL/6-Tg(Csf1r-EGFP-NGFR/FKBP1A/TNFRSF6)2Bck/J (MaFIA) and B6.129P2-Nos2tm1Lau/J (*Nos2*$^{-/-}$) transgenic mice were bred in our animal facility. All mice were housed under SPF conditions, sex-matched and aged between 6 and 10 weeks for each experiment. All procedures were performed in agreement with the Institut Pasteur institutional guidelines for animal care. Experimental protocols were approved by the Animal Ethics Committee #1 of the Comité Régional d'Éthique pour l'Expérimentation Animale (CREEA), Ile-de-France (MESR N° 01264).

Parasites

DsRed-expressing *Leishmania major* parasites were grown at 26°C for a maximum of 5 passages in M119 medium supplemented with 10% heat-inactivated fetal bovine serum, 0.1 mM adenine, 1 µg/mL biotin, 5 µg/mL hemin and 2 µg/mL biopterin.

Bone marrow-derived macrophages (BMDMs)

Femurs and tibias were isolated from adult WT or *Nos2*$^{-/-}$ mice, sterilized in 70% ethanol and flushed with PBS. Single cell suspensions were prepared by filtering the marrow through a 30 µm cell strainer. 20×10^6 BMC were cultured in 150 mm non-treated Petri dishes for 7 days, 37°C, 5% CO_2, in 30 mL RPMI medium 1640 - GlutaMAX™ supplemented with 10% heat-inactivated fetal bovine serum, 100 U/mL penicillin, 100 ng/mL streptomycin, 1 mM sodium pyruvate, 1 mM HEPES and 5 mM 2-mercaptoethanol (complete RPMI) and 20% L929-cell conditioned supernatant. 30 mL of fresh medium was added 3 days after plating.

Method details

Infection, inflammation model and L-NIL treatment

For infection, stationary-phase promastigotes were resuspended at 10^8 parasites/mL in PBS and 5 µL were injected intradermally into the ear dermis. To induce a non-infectious inflammatory reaction, incomplete Freund's adjuvant was emulsified with an equal volume of saline and 10 µL were injected intradermally into the ear dermis. To inhibit iNOS activity, L-NIL was freshly prepared at 2 mg/mL in PBS and mice were injected with 100 µL i.p. once a day for 3 days, starting 14 days post infection or 4 days post challenge. Age and sex-matched controls were infected or challenged at the same time and did not received L-NIL injection.

Extraction of ear cells

Ears harvested from euthanized mice were separated into dorsal and ventral sheets using tissue forceps before being digested for 45 min, 37°C, 700 rpm, in RPMI medium 1640 supplemented with 100 U/mL penicillin, 100 ng/mL streptomycin, 0.5 mg/mL liberase TL and 50 ng/mL DNase. Single cell suspensions in PBS were prepared by crushing digested ears into a 70 µm cell strainer. After a washing step in PBS and filtration, cells were analyzed by flow cytometry or subjected to extracellular flux analysis.

Adoptive transfer

Bone marrow cells were harvested from Ubi-GFP mice and filtered through a 30 µm cell strainer to generate a single cell suspension. 6×10^7 cells were injected i.v. per mice after anaesthesia.

Flow cytometry

In vitro generated BMDMs were washed with cold PBS and incubated for 10 min, 4°C, in 3 mL of Cell Dissociation Buffer to detach the cells. BMDMs were recovered by adding 10 mL of cold PBS and washed before seeding at 10^6 cells/well (6-well non-treated plates) in 2 mL complete RPMI supplemented with 20% L929-cell conditioned supernatant. To vary the density of iNOS competent cells in the culture, we mixed WT and *Nos2*$^{-/-}$ BMDMs at various ratios, keeping the total cell number constant to avoid confounding effects of varying cytokine and/or nutrients concentrations. The day after seeding, medium was removed and replaced with 2 mL of fresh complete RPMI supplemented with 1 µg/mL LPS + 50 ng/mL IFN-γ for activation. When needed, treatment with 20 µg/mL L-NIL was performed at the time of activation. Treatment with oligomycin or azide was performed 20 h post activation at the indicated doses. To monitor glucose uptake, 20 µM 2-deoxy-2-[(7-nitro-2,1,3-benzoxadiazol-4-yl)amino]-D-glucose (2-NBDG) was incubated with cells during 1 h. 24 h post activation,

BMDMs were washed with cold PBS and incubated for 10 min, 4°C, in 300 µL Cell Dissociation Buffer to detach the cells. BMDMs were harvested by adding 1 mL of cold PBS to each well. Cells were stained with Zombie Violet fixable dye diluted at 1:200 in PBS supplemented with 2% FBS and 5 mM EDTA (FACS buffer) for 15 min, 4°C, to assess cell viability. BMDMs were stained for 15 min, 4°C, in FACS buffer supplemented with 10 µg/mL anti-mouse CD16/32 (Fc-block) using a combination of fluorescently-labeled monoclonal antibodies among: PerCP-Cy5.5 anti-CD11b, APC-eFluor® 780 anti-MHC II (I-A/I-E). For intracellular staining, prior harvesting the cells, BD GolgiPlug diluted at 1:1000 was added to every well without volume variation, 20 h post activation. Cells were harvested and stained as described above. BMDMs were fixed for 30 min, 4°C, using formaldehyde solution diluted at 2% in PBS. Cells were permeabilized using PermWash buffer following manufacturer's instructions and stained for 45 min, 4°C, using a combination of fluorescently-labeled monoclonal antibodies among: PE anti-mouse CCL2, PE anti-mouse CCL3, APC anti-mouse IL-1β Pro-form.

For *ex vivo* analyses, extracted ear cells were stained with Zombie Violet fixable dye diluted at 1:200 or LIVE/DEAD blue fixable dye diluted at 1:500 in FACS buffer for 15 min, 4°C, to assess cell viability. Cells were then fixed for 30 min, 4°C, using formaldehyde solution diluted to 2% in PBS. Surface staining of cells was performed for 15 min, 4°C, in FACS buffer supplemented with 10 µg/mL anti-mouse CD16/32 (Fc-block) using a combination of fluorescently-labeled monoclonal antibodies among: BUV395 anti-CD45, BV421 anti-MHC II (I-A/I-E), BV510 anti-Gr-1, BV510 anti-Ly-6G, BV605 anti-Ly-6C, PerCP-Cy5.5 anti-CD11b, PE-Cy7 anti-CD45.1, APC anti-CD11c, APC-eFluor® 780 anti-CD45.2, APC-eFluor® 780 anti-MHC II (I-A/I-E). For intracellular staining, extracted cells were plated in 48-well plates in 1 mL complete RPMI supplemented with BD GolgiPlug (diluted at 1:1000) for 4 h, 37°C. iNOS inhibition was maintained adding 20 µg/mL L-NIL to dedicated wells.

Cells were harvested by flushing all wells and submitted to staining as described above. After surface staining, cells were permeabilized using PermWash buffer following manufacturer's instructions and stained 45 min, 4°C, using a combination of fluorescently-labeled monoclonal antibodies among: Alexa Fluor® 488 anti-mouse TNF-α, eFluor® 660 anti-CCL3, APC anti-mouse IL-1β Pro-form. Samples were analyzed using a BD CantoII or a BD Fortessa flow cytometer equipped with FACSDiva software (BD Bioscience) or a CytoFLEX LX flow cytometer equipped with CytExpert software (Beckman Coulter).

For analysis of PercevalHR-expressing cells, two fluorescence signals were acquired. F_{low} was collected by exciting PercevalHR with a violet laser (λ_{low} = 405 nm) and filtering the signal through a 525/40 filter. F_{high} was collected by exciting PercevalHR with a blue laser (λ_{high} = 488 nm) and filtering the signal through a 510/20+OD1 filter. Cellular ATP:ADP ratio was determined by calculating F_{high}:F_{low} ratio for each acquired cell. For time-resolved (kinetic) flow cytometry, ATP:ADP ratio was normalized to the first value acquired (t_0). Data analysis was performed using FlowJo 10.2 software.

MitoTracker staining

After activation, cells were loaded with MitoTracker® dyes using 40 nM MitoTracker® GreenFM and 50 nM MitoTracker® Red CMXRos during 30 min, 37°C, 5% CO_2. Cells were washed with cold PBS before flow cytometry analysis.

Hypoxic culture

Hypoxic cultures were conducted using PetakaG3 FLAT hypoxic devices (balancing the partial pressure of dissolved oxygen in the media at 25 mmHg). 15×10^6 BMDMs were loaded into each chamber in 20 mL complete RPMI supplemented with 20% L929-cell conditioned medium and cultivated horizontally overnight to allow cell seeding. The day after, medium

was replaced for activation. Cell treatments and flow cytometry were performed as described earlier.

Extracellular flux analysis

BMDMs were analyzed using an XF^{e}96 Extracellular Flux Analyzer (Seahorse Bioscience). BMDMs were plated in XF^{e}96 cell culture microplates (10^5 cells/well in 200 µL final) and either left untreated or activated with 1 µg/mL LPS + 50 ng/mL IFN-γ, 37°C, 5% CO_2. 24 h post activation, cells were washed with XF Base medium supplemented with 10 mM glucose, 2 mM glutamine and 1 mM sodium pyruvate (MitoStress XF running buffer, pH adjusted to 7.4) or supplemented with 2 mM glutamine (GlycoStress XF running buffer, pH adjusted to 7.4), and 175 µL of appropriate XF running buffer was added as final volume. BMDMs were stored 1 h at 37°C in a non-CO_2 incubator before starting the analysis. Following manufacturer's instruction, OCR and ECAR were measured in response to 1 µM oligomycin, 1.5 µM Carbonyl cyanide-*4*-(trifluoromethoxy)phenylhydrazone (FCCP) and 0.5 µM rotenone and antimycin A (MitoStress Test Kit) or in response to 10 mM glucose, 1 µM oligomycin and 50 mM 2-deoxy-glucose (2-DG) (GlycoStress Test Kit).

For *ex vivo* isolation of mononuclear phagocytes from infected ears, we relied on the expression of the CD11c marker on both P2 and P3 populations (Olekhnovitch et al., 2014). $CD11c^+$ cells were isolated from infected ears using positive selection on MACS columns. The isolated population contained at least 90% of $CD11b^+MHC\text{-}II^+$ monocyte-derived cells. Cells were washed and plated at 10^5 cells/well in 175 µL of MitoStress XF running buffer and treated with 20 µg/mL L-NIL or left untreated during 2 h, 37°C, non-CO_2 incubator. Following manufacturer's instruction, OCR and ECAR were measured in response to 1 µM oligomycin, 1.5 µM FCCP and 0.5 µM rotenone and antimycin A (MitoStress Test Kit).

Data analysis was performed using Wave software.

Multiplex assay for cytokine and chemokine quantification

Ears harvested from euthanized mice were separated into dorsal and ventral sheets and snap frozen before storage at -80°C until analysis. For tissue lysates preparation, ears were thawed out and chopped in 1 mL RIPA buffer on ice. After 20 min incubation, samples were grounded during 2 min with a Potter-Elvehjem PTFE pestle into an appropriate glass tube. Lysates were subsequently clarified by centrifugation for 15 min at 4°C, 15.000 rcf. Multiplex assay was performed following manufacturer's instructions. Lysates were diluted at 1:2 in assay diluent. Standards were reconstituted with RIPA buffer diluted at 1:2 in assay diluent. For analyte capture, the plate was incubated overnight at 4°C under agitation on an orbital shaker. Plate reading was performed using a Bio-Plex 200 system equipped with Bio-Plex Manager software (Bio-Rad).

For *in vitro* analyses, BMDMs were cultivated and activated as indicated during 24 h. Supernatants were harvested and cleared by centrifugation before being snap frozen and stored at -80°C until analysis. The day of analysis, supernatants were diluted 1:4 in assay diluent and multiplex assay was performed as described previously.

PercevalHR probe and virus generation

The original PercevalHR construct was cloned into a murine stem cell viral (MSCV) vector. HEK 293 cells were co-transfected with 6 µg pMSCV-PercevalHR and 4 µg pCL-Eco plasmids using JetPRIME reagent following manufacturer instructions. Medium was changed 4 h after with complete RPMI. 48 h after transfection, retrovirus containing supernatant was harvested from HEK 293 cells, 0.45 µm-filtered and supplemented with 10 µg/mL polybrene to generate retroviral-conditioned medium.

Retroviral transduction of BMDMs

BMDMs were retrovirally transduced during their differentiation. On day 3, differentiation medium was exchanged with 25 mL retroviral-conditioned medium supplemented with 20% L929-cell conditioned medium for an overnight incubation. On day 4, retroviral medium was replaced with complete RPMI supplemented with 20% L929-cell conditioned supernatant for an additional 3 days. Transduction efficiencies of >60% were routinely achieved.

Generation of mixed-bone marrow chimeras

WT CD45.1 recipient mice were γ-irradiated with a single lethal dose of 9 *Gy*. Femurs and tibias were isolated from adult WT CD45.1 or *Nos2*$^{-/-}$ CD45.2 mice, sterilized in 70% ethanol and flushed with PBS. Single cell suspensions were prepared by filtering the marrow through a 30 μm cell strainer. Mice were anaesthetized 2 hours post irradiation and reconstituted with a total of 5×10^7 bone marrow cells (WT, *Nos2*$^{-/-}$ or a mixture of both) by retro-orbital i.v. injection. Chimeras were infected 6 to 8 weeks after reconstitution. The same protocol was used to generate mixed-bone marrow chimeras using WT and MAFIA cells.

Generation of PercevalHR-expressing fetal liver chimeras

WT recipient mice were γ-irradiated with a single lethal dose of 9 *Gy*. Mice were anaesthetized 2 hours post irradiation and reconstituted with a total of 1×10^6 PercevalHR-expressing fetal HSCs plus 5×10^5 WT bone marrow cells by retro-orbital i.v. injection. For PercevalHR-expressing HSC generation, fetal liver of E14.5 embryos were harvested and multipotent HSCs were isolated by negative selection on MACS columns using biotin anti-mouse TER-119 antibody. Isolated HSCs were cultivated overnight in complete RPMI supplemented with 200 ng/mL rmSCF, 200 ng/mL rmFlt3-L and 200 ng/mL rmIL-3 at a density of 1×10^6 cells/mL. The day after, 1×10^6 HSCs in 2 mL retroviral-conditioned medium

were retrovirally transduced by spin infection (800 *g*, 2 h, 32°C). After the spin infection, medium was replaced with complete RPMI supplemented with the same cytokine cocktail for an overnight incubation before injection into irradiated recipients. Chimeras were infected 8 weeks after reconstitution.

Intravital imaging

Mice were anaesthetized and prepared for intravital two-photon imaging. Each mouse was placed on a custom-designed heated stage, one ear was placed onto a metal piece and immobilized with double sided tape. The ear was kept moisturized using ophthalmic gel covered by a coverslip. Two-photon imaging was performed using a 25X/1.05 NA objective (Olympus) immerged in deionized water and installed into a DM6000 upright microscope equipped with a SP5 confocal head (Leica Microsystem) and a Chameleon Ultra Ti::Sapphire Laser (Coherent) tuned at 920 nm. Emitted fluorescence was split with dichroic mirrors (Semrock) and filtered with appropriate filters (Semrock) for each channel before collection with nondescanned detectors. Typically, images from 15 to 20 z planes spaced by 5 µm were collected every 2 minutes for up to 3 hours. For *in vitro* analysis of PercevalHR-expressing BMDMs, two-photon imaging was performed using a 25X/1.05 NA objective (Olympus) installed into a FVMPE-RS upright microscope (Olympus) equipped with an Insight deep see dual laser (Spectra physics) and a resonant scanner. PercevalHR excitation was achieved using λ_{low} = 830 nm and λ_{high} = 1040 nm. Emitted fluorescence, collected sequentially for each λ, was split with dichroic mirrors (Semrock) and filtered with a 520/35 filter (PercevalHR signal) and a 483/32 filter (background) before collection with GaAsP detectors. Images in a single plan were collected every 15 s for 5 to 10 min. Data collected were analyzed and processed using Fiji (ImageJ) and Imaris software.

Quantification and statistical analysis

Data are reported as the mean ± SD, and numbers of experiments are reported in figure legends. For *in vitro* analyses, statistical differences between two groups were evaluated using a two-tailed unpaired Student's t-test with Welch's correction or using an ordinary one-way ANOVA with post hoc Holm-Sidak test for multiple comparison. For *in vivo* analyses, unless indicated otherwise, statistical differences between two groups were evaluated using a Mann-Whitney U test. Correlation between the density of iNOS competent cell and cellular respiration and cytokine production was further analyzed *in vitro* and *in vivo* by exponential one-phase decay regression. Significance was defined by a p-value<0.05. All statistical tests were performed using GraphPad Prism 6.0a software. p-values were reported as stars: * $p<0.05$; ** $p<0.01$; *** $p<0.005$

Postat et al.
Figure 1

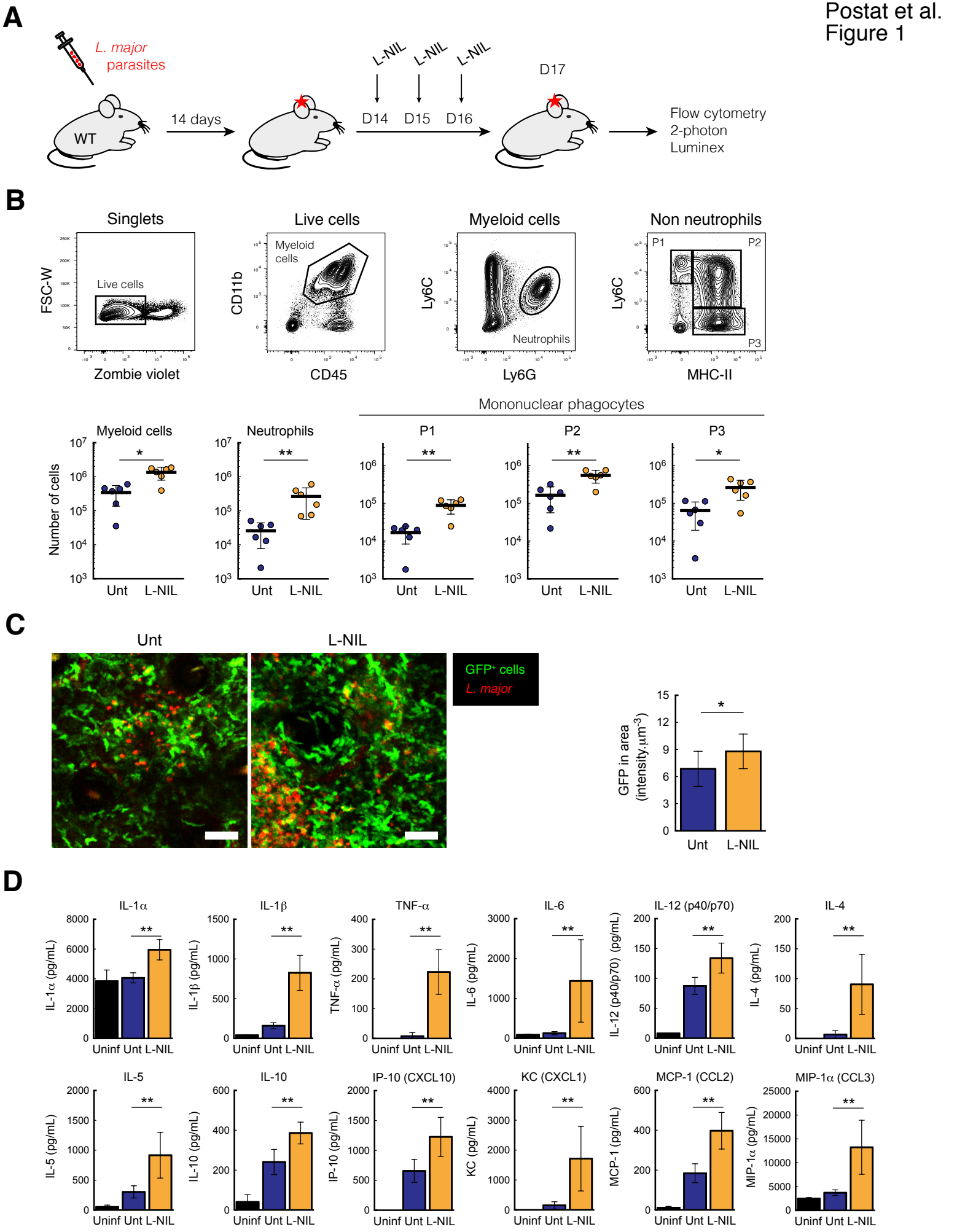

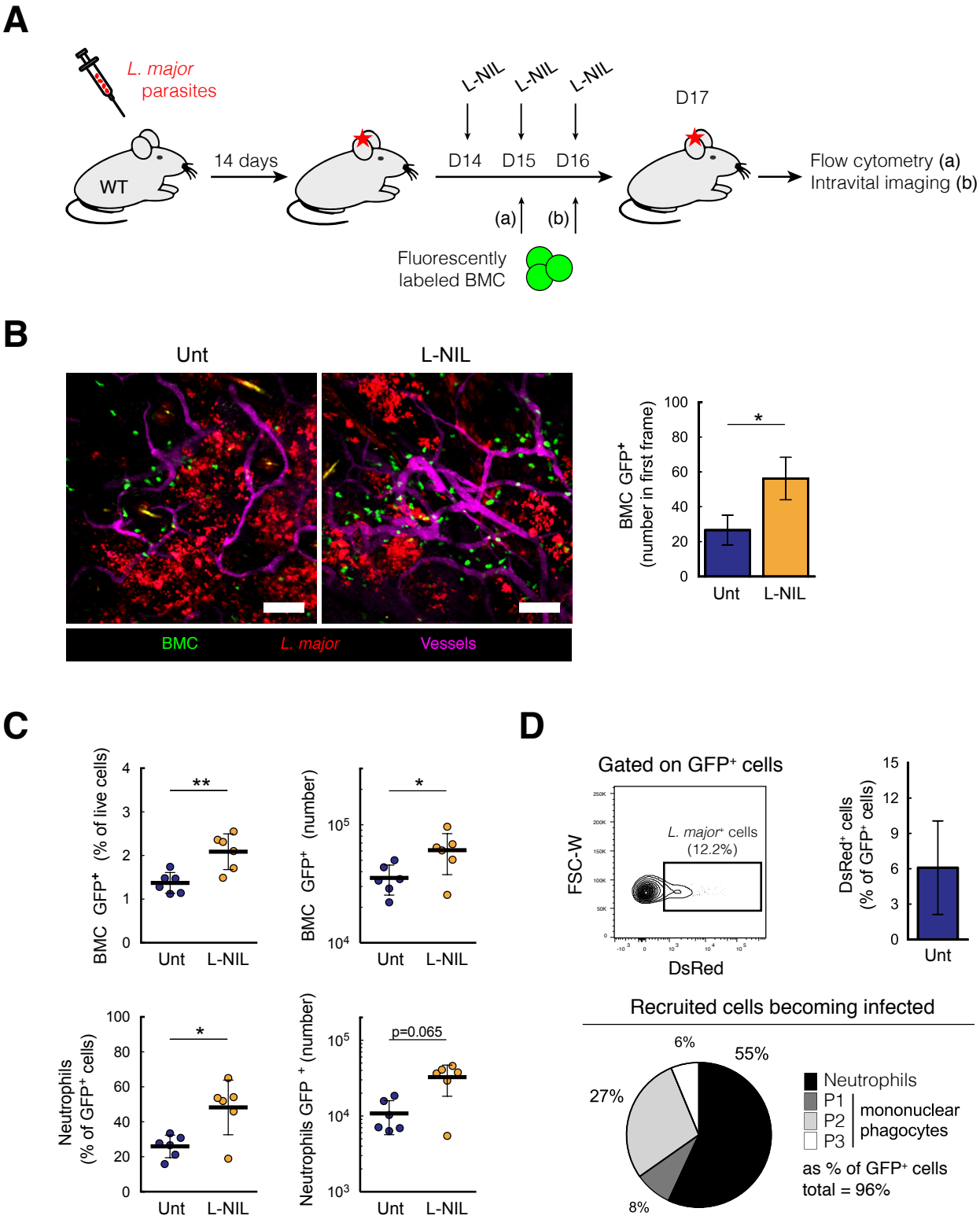
A
L. major parasites
WT
14 days
L-NIL
L-NIL
L-NIL
D14
D15
D16
D17
(a)
(b)
Flow cytometry (a)
Intravital imaging (b)
Fluorescently labeled BMC
B
Unt
L-NIL
BMC
L. major
Vessels
BMC GFP+ (number in first frame)
Unt
L-NIL
C
BMC GFP+ (% of live cells)
BMC GFP+ (number)
Neutrophils (% of GFP+ cells)
Neutrophils GFP + (number)
p=0.065
D
Gated on GFP+ cells
L. major+ cells (12.2%)
FSC-W
DsRed
DsRed+ cells (% of GFP+ cells)
Recruited cells becoming infected
6%
55%
27%
8%
Neutrophils
P1
P2
P3
mononuclear phagocytes
as % of GFP+ cells
total = 96%

Postat et al.
Figure 3

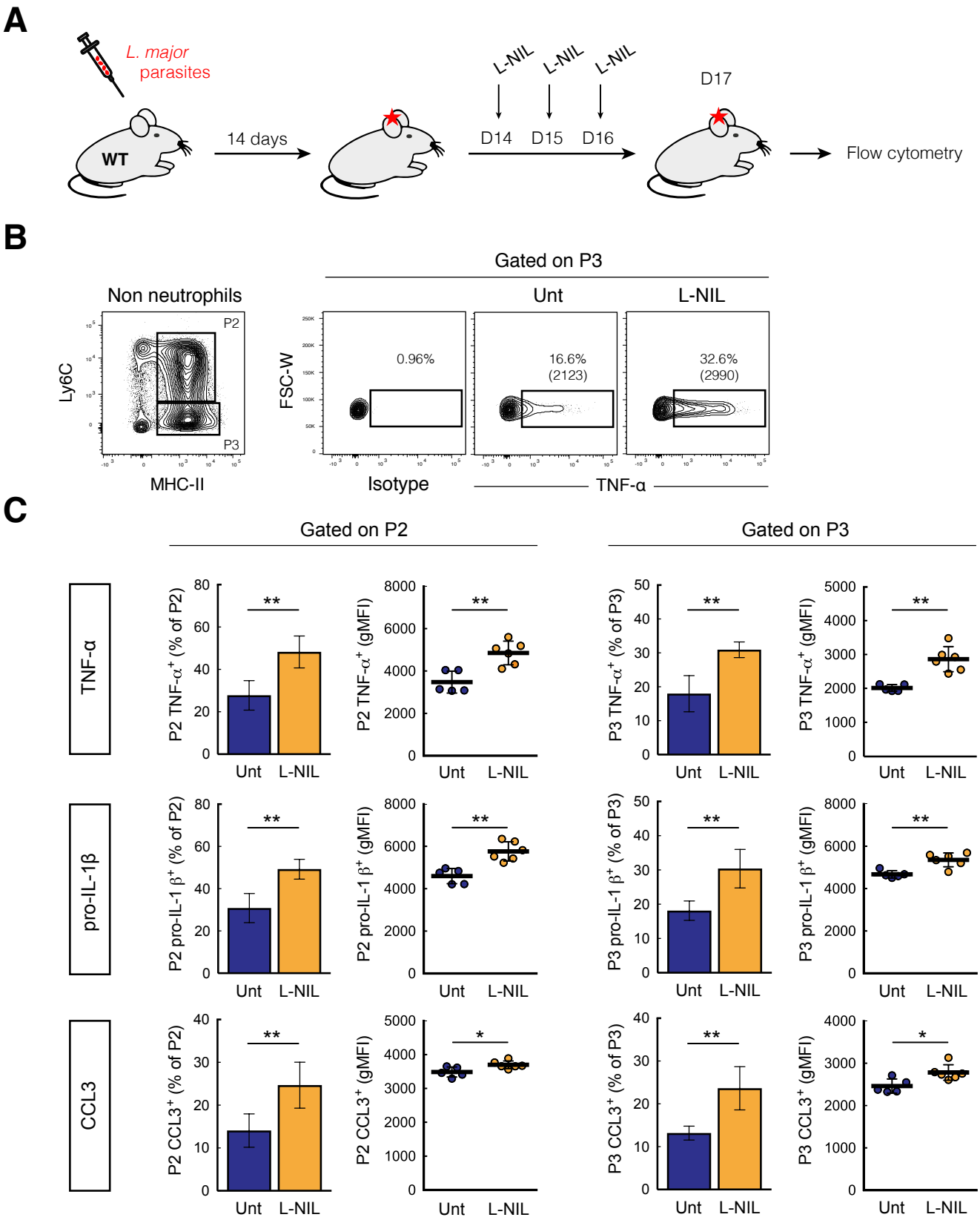

Postat et al.
Figure 4

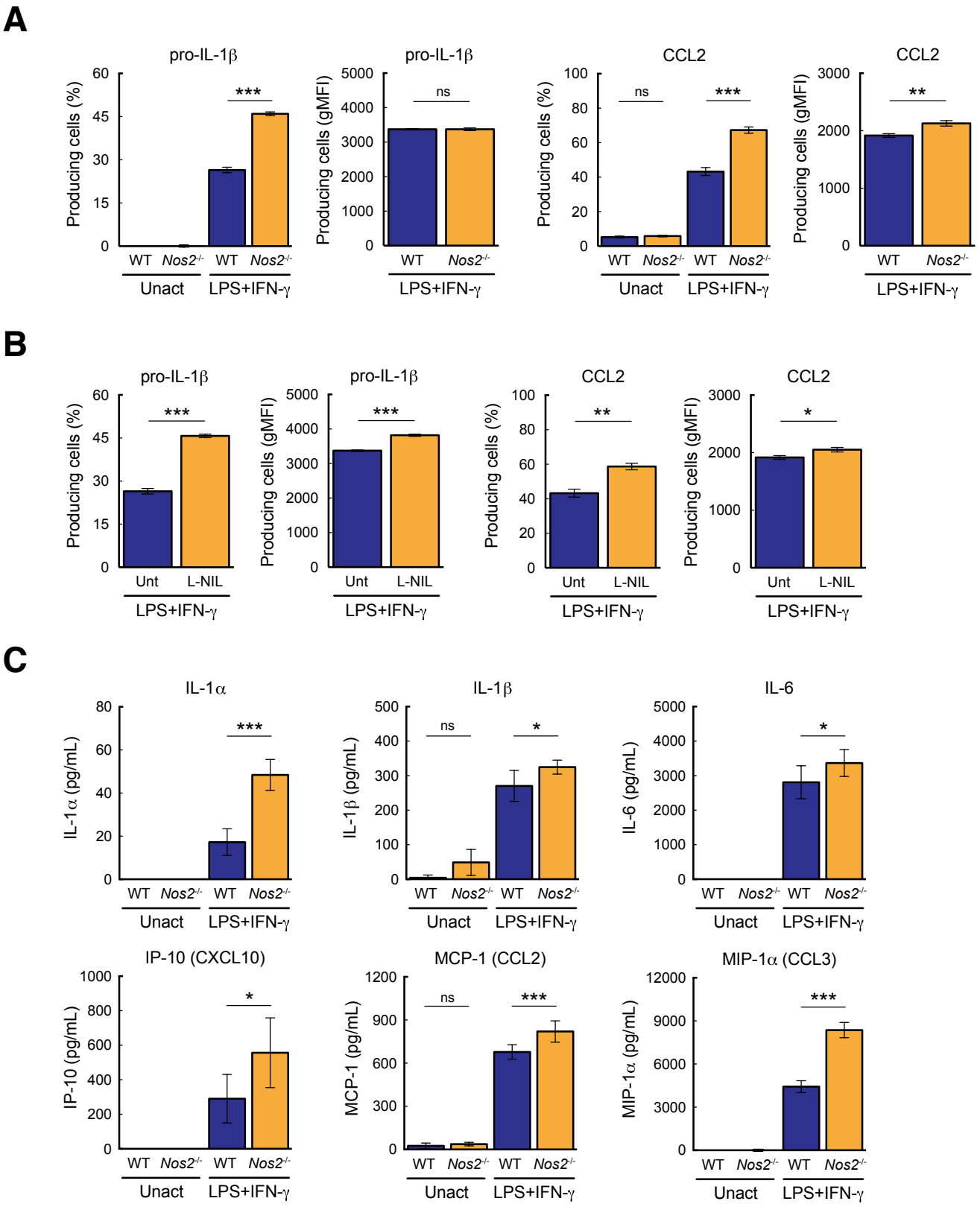

Postat et al.
Figure 5

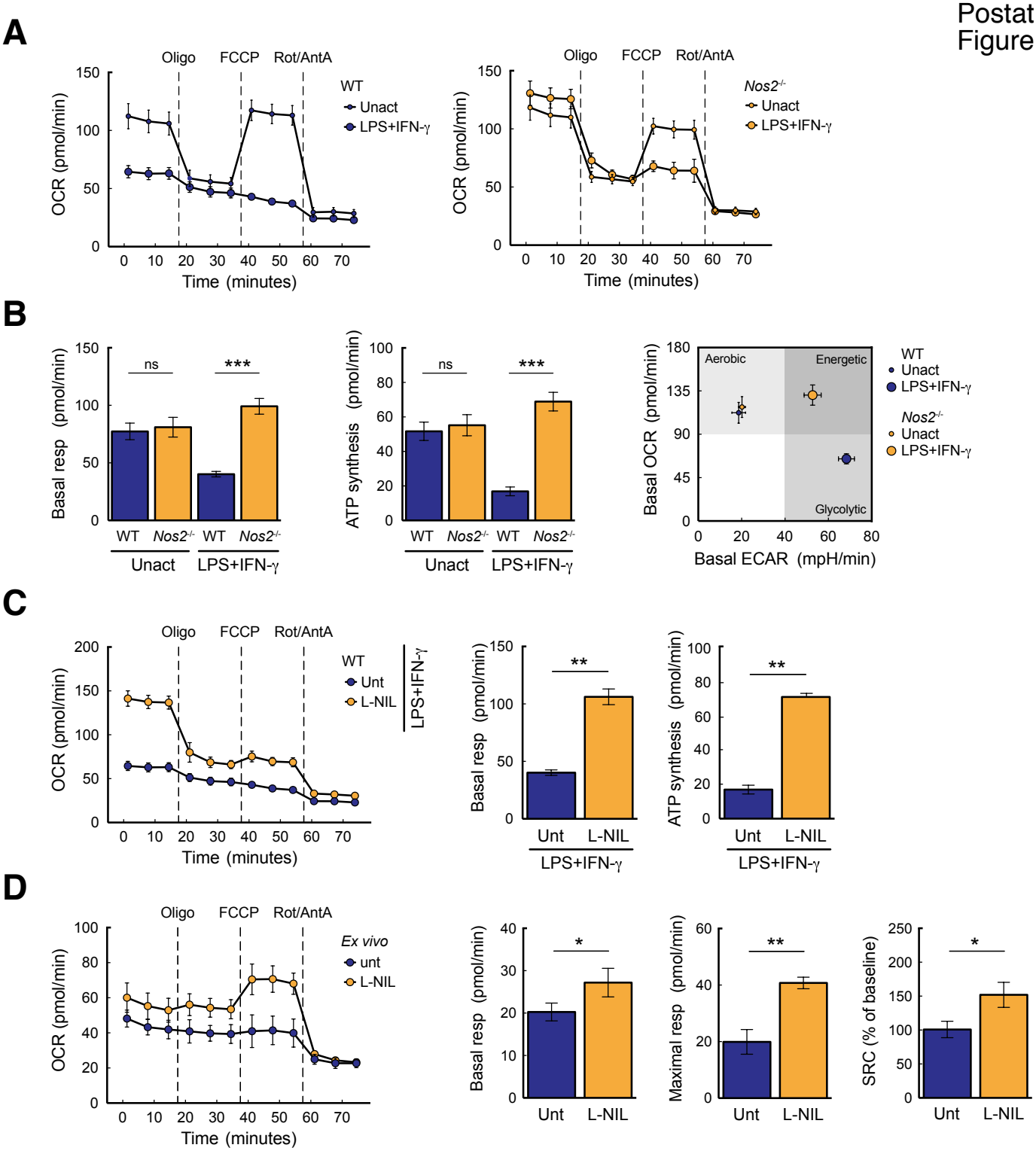

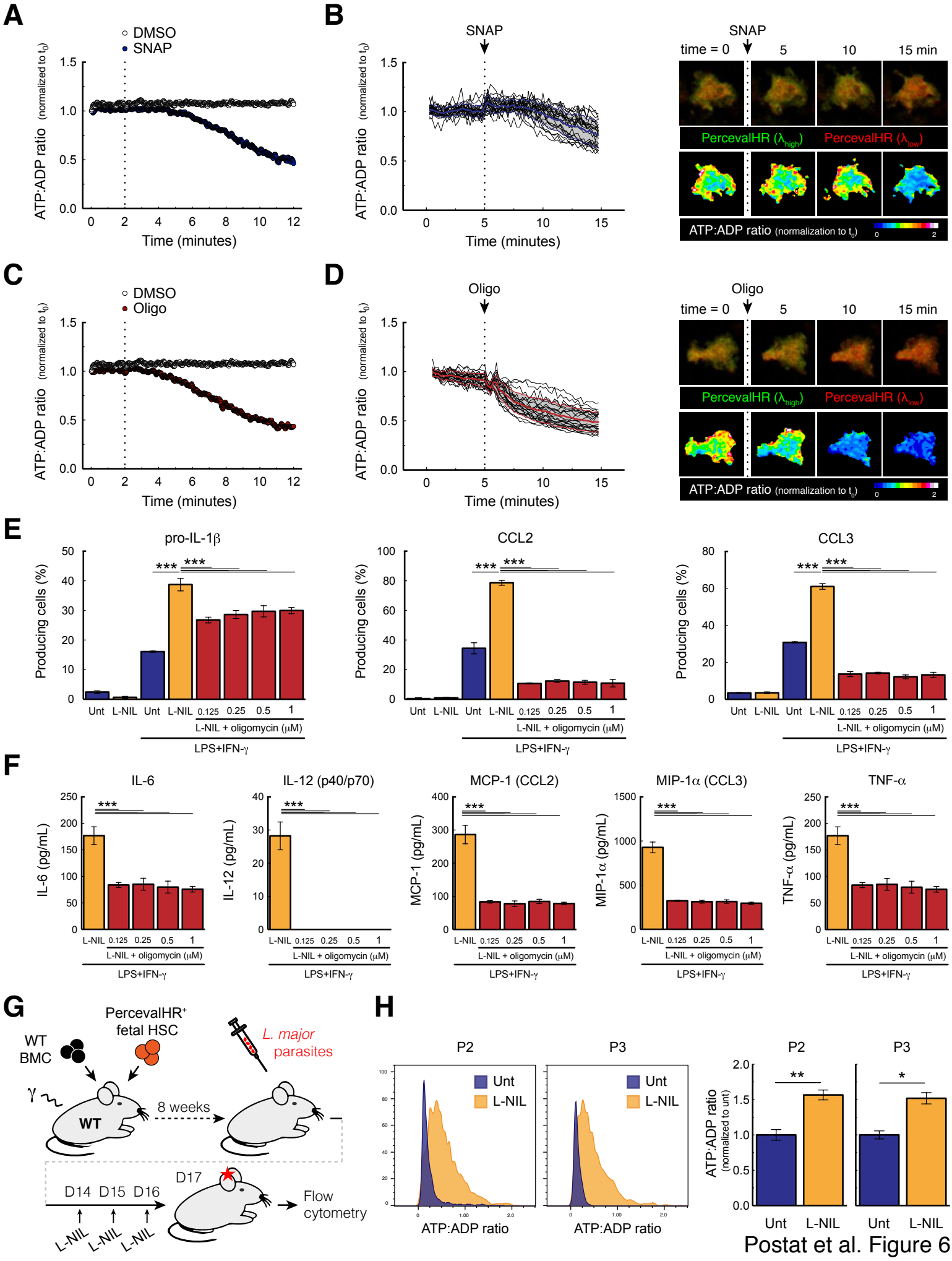

Postat et al. Figure 6

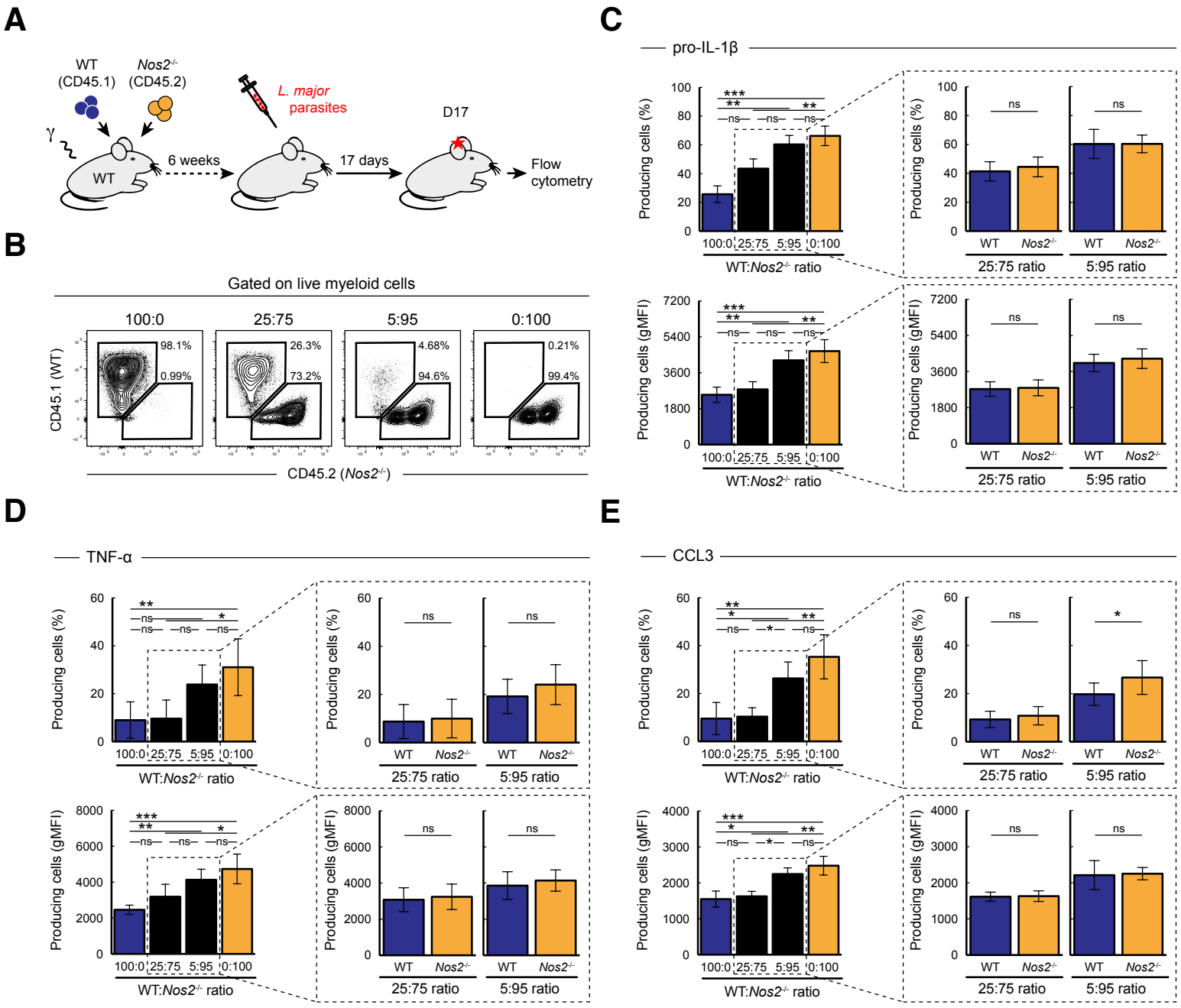

Postat et al. Figure 7